Characterization of Steady-State Current Ripple in Interleaved Power Converters Under Inductance Mismatches

Pablo D. Antoszczuk, *Student Member, IEEE*, Rogelio Garcia Retegui, *Member, IEEE*, Nicolas Wassinger, *Student Member, IEEE*, Sebastian Maestri, Marcos Funes, *Member, IEEE*, and Mario Benedetti

***Abstract*—Interleaved power converters are used in high-current applications due to their inherent reduction of semiconductors stress and total ripple. Ripple reduction is accomplished by a correct phase shifting, and the filtering improvement explained by the increase in the ripple frequency. However, these benefits are wasted, among other reasons, by the mismatch of the phase inductor value. As a consequence, differences in the ripple amplitude among phases are produced, leading to a total current ripple significantly greater than the ideal case, the loss of the cancellation points and the generation of the switching frequency component and its harmonics. The works dealing with this subject matter have focused on particular cases, such as a given number of phases, a specific converter topology, or a particular case of inductance mismatch, disregarding a general analytical approach. This paper proposes an analytical method to characterize the total ripple in steady state as a function of the duty cycle and the number of phases under any condition on inductance mismatch. Experimental results validate the proposed method.**

***Index Terms*—Current ripple, inductance tolerance, interleaved power converters.**

I. Introduction

In applications where the efficient control of high currents is required, like in grid-connected inverters, automotive applications, PFC converters, voltage regulator modules, and high-power applications, the use of an interleaved power converter is the most convenient solution [1]–[6]. The use of N phases allows the distribution of high current among phases, thereby reducing the conduction and commutation losses of switching devices. The control of said devices permits to interleave the phases ripples in such a way that their sum, defined as a total ripple, is minimized. Under ideal conditions, the amplitude, duty cycle, and frequency are the same for all phases, and the phase shift is $\frac{2\pi}{N}$. Consequently, the frequency of the total ripple is increased to N times the switching frequency f_{sw}, which allows us to improve the filtering of the total current [7]–[9].

The benefits aforementioned are affected by tolerances and nonidealities in passive and active components (like switch on-resistance, driver delays, inductor parasitic resistance, and inductor values) [10], [11]. Most of these nonidealities cause dc current unbalance among phases, which can be mitigated by means of digital control [12]–[15]. Regarding the total ripple, its minimization deteriorates with respect to the ideal case due to two main causes: 1) improper phase shift among the different phase currents, and 2) differences between the peak amplitude of the phase currents. The error in the phase shift may be the result of the different turn-on delays in the switches, which leads to a total current ripple degradation that worsens as the difference between the time delays is comparable to the commutation period $T = f_{sw}^{-1}$ [16]. Even though phase-shift errors could generate remarkable differences on total ripple cancellation, there are strategies to mitigate these effects [4], [17]–[19]. With respect to the differences between the peak amplitude of the phase currents, the main cause is phase inductance mismatch. The origin of this mismatch may differ depending on whether ungapped or gapped inductors are analyzed. In the case of ungapped inductors, the most important causes of mismatch are tolerances in the magnetic permeability (usually $\pm 5\%, \pm 10\%$ for iron powder cores) and differences in the winding process (such as winding mechanical pressure or distribution) [20]. In the case of gapped inductors, the main cause of inductance mismatch is given by gap size tolerance, which is more critical in small gaps. The design-specified gap may change for several reasons, among them: tolerance in the grinding process if the gap is machined, thickness of the glue used to clamp the two core halves, or shrinking of potting material as it cures. Provided these considerations are taken into account, inductance tolerances within $\pm 10\%$ could be expected in a standard design [21].

Unlike the case of phase-shift error, mismatches among inductances generate differences in the current ripple amplitude among phases that cannot be eliminated by means of control strategies [22]. Compared to the ideal condition, under inductance mismatches, the total current ripple becomes significantly greater, and the switching frequency component and its harmonics are not canceled, which impacts on the overall system performance. For instance, the output capacitance in an interleaved buck converter must be sized based on the increased current ripple and lower frequency components, leading to an

Manuscript received April 8, 2013; revised June 4, 2013; accepted June 10, 2013. Date of current version October 15, 2013. This work was supported in part by the Universidad Nacional de Mar del Plata, Argentina, the National Scientific and Technical Research Council, Argentina, the Ministry of Science, Technology and Productive Innovation, Argentina, the National Agency of Scientific and Technological Promotion, Argentina, the European Organization for Nuclear Research, Switzerland, and the European Particle Physics Latin American Network. Recommended for publication by Associate Editor J. A. Cobos.

The authors are with the Instrumentation and Control Laboratory, Universidad Nacional de Mar del Plata, B7600, Mar del Plata, Argentina (e-mail: pablo_ant@fi.mdp.edu.ar; rgarcia@fi.mdp.edu.ar; nwassinger@fi.mdp.edu.ar; somaestri@fi.mdp.edu.ar; mfunes@fi.mdp.edu.ar; mbenedet@fi.mdp.edu.ar).

Digital Object Identifier 10.1109/TPEL.2013.2270005

increase in the capacitance value. With regard to the analysis of total current ripple due to inductance mismatches, only particular cases have been reported, such as a given number of phases, a specific converter topology, or a particular case of difference between inductances [16], [22]–[24]. Yet a general analytical approach remains to be determined.

This paper proposes a method to characterize the total current ripple in steady state as a function of the duty cycle for N-phase interleaved power converters under any condition on inductance mismatch. The characterization of the total current ripple is performed by analyzing the peak values of this current ripple, and the instant when these peak values appear. The proposed methodology leads to general analytical expressions that allow us to numerically evaluate different characteristics related to the total current ripple for the whole range of the duty cycle. This avoids simulating the converter for each value of the duty cycle. By using this approach, expressions for the maximum amplitude, RMS value, and harmonic content of the total current ripple, and the amplitude of the voltage ripple across the capacitor connected to the common connection point of the phases can be computed. These expressions were computed and verified with measurements on a three-phase interleaved buck converter.

II. Proposed Method

The proposed method characterizes the total current ripple in the interleaved power converters (i.e., the current ripple at the input in a boost converter or at the output in a buck converter), based on the analysis of each phase ripple in the time domain. To carry out this analysis, the following is assumed:

1) the interleaved power converter is operating in steady-state and continuous-conduction mode;
2) the voltage drop of the semiconductor devices and parasitic resistances among phases are similar, thus, the duty cycle D is the same for all phases;
3) the time constant, associated with the inductors and their resistive component, is usually much higher than the switching period, thus, the phase current can be approximated by linear segments;
4) the phase errors among phases, with respect to the ideal phase shift $\left(\frac{2\pi}{N}\right)$, are small compared to the switching period; therefore, they are neglected.

Under these conditions, the possible differences in the ripple amplitude depend mainly on inductances tolerance. Moreover, given the linear approximation of the phase current waveform, the ripple of each phase current is defined by the peak values of the ripple and the instant in which these peaks appear.

Fig. 1 shows an example of the normalized phase current ripples, $r(t)$, and the total current ripple, $r_{_T}(t)$, of an interleaved power converter with inductance mismatches. The aim of this figure is to illustrate a starting point to develop the ripple characterization based on a general case. As it can be observed, due to the ripple waveform, the peaks in the total ripple occur at the same time instant than the peaks in the phases ripple. These peaks are named positive (negative) when the current slope changes from positive to negative (from negative to positive). In the case of a positive (negative) peak the superscript $+$ $(-)$ is used. Hence, P_x^+ (P_x^-) is the peak of the total current ripple when a positive (negative) peak in the phase x occurs.

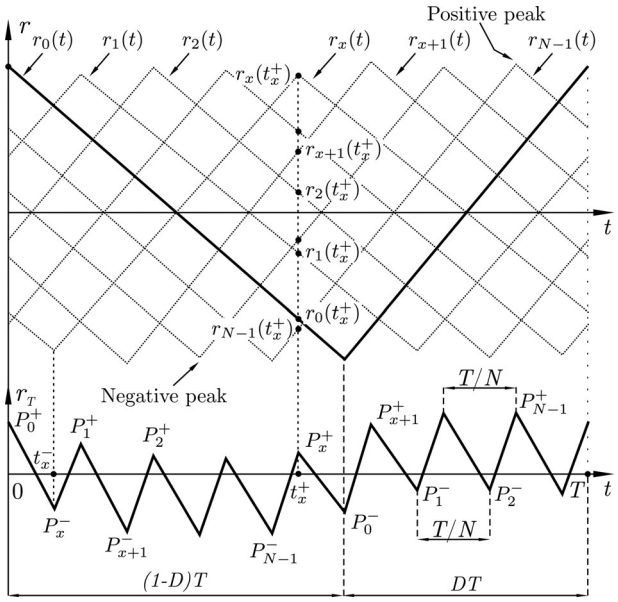

Fig. 1. Interleaved power converter. Normalized phase (top) and total current ripple (bottom).

In the figure, a generic positive peak P_x^+, which occurs at time t_x^+, can be computed as

$$P_x^+ = r_0(t_x^+) + r_1(t_x^+) + \cdots + r_x(t_x^+) \cdots r_{N-1}(t_x^+) \quad (1)$$

where $r_x(t_x^+)$ is the phase current ripple of the phase x in time t_x^+.

The time instants $t_x^{\pm}$ are related to the occurrence of positive and negative peaks in the phase currents. Since the time when these peaks occur can be analytically calculated, the instants of the peaks in the total current can be precisely defined. In Fig. 1, it can be seen that the time elapsing between positive (negative) peaks in the phase or the total ripple is constant and equals $\frac{T}{N}$. If the time at which the positive peak of phase 0 (P_0^+) occurs is taken as a reference, the time at which the peak associated with a generic phase x, t_x^+, occurs is equal to $\frac{xT}{N}$. It can also be noticed that the time instant at which the negative peak of phase x, t_x^-, occurs is equal to $\frac{xT}{N} - DT$. Notice that, due to the periodicity of the system, t_x^- is equal to $\frac{xT}{N} - DT + T$, when $\frac{xT}{N} - DT$ is negative.

In order to calculate the value of the phase current ripples when a positive or negative peak occurs in any of the phases, a generic representation of the phase current ripples is proposed, based on the system symmetry and periodicity. In this representation, the current ripple of a given phase x is defined as a triangular shaped function $f(t)$ of period T weighed by a normalized amplitude A_x

$$r_x(t) = A_x f(t) = \frac{\hat{I}_x}{\hat{I}_n} f(t) \quad (2)$$

where $\hat{I}_x$ and $\hat{I}_n$ are the maximum ripple amplitudes associated with phase x and the nominal amplitude, respectively. These

TABLE I
PHASE PEAK AMPLITUDE AS A FUNCTION OF THE DUTY CYCLE

	$\hat{I}_x$	$\hat{I}_n$
Boost	$\frac{V_i DT}{2L_x}$	$\frac{V_i DT}{2L_n}$
Buck	$\frac{V_i(1-D)DT}{2L_x}$	$\frac{V_i(1-D)DT}{2L_n}$

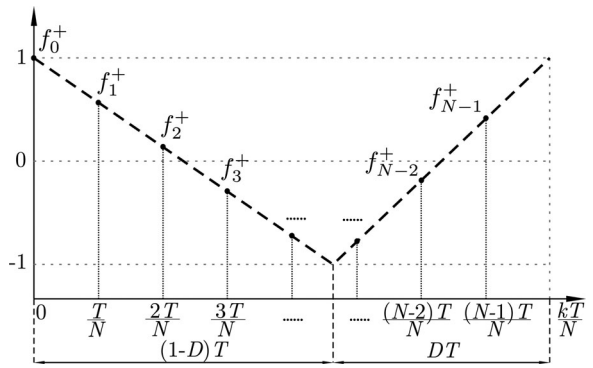

Fig. 2. $f^+(t)$ (dashed line) and f_k^+ (dots).

amplitudes are a function of the duty cycle and the type of converter used, as shown in Table I.

In Table I, L_x is the inductance associated with the phase x and L_n is the nominal inductance, which is defined based on the design specification. The remaining phases are generated using a delayed version of $f(t)$ weighed by their corresponding normalized amplitude.

In order to calculate P^+, it is convenient to express the function $f(t)$ with its maximum positive at $t = 0$. This function, named $f^+(t)$, is represented by two sections with different slopes, separated by the instant $t = (1 - D)T$, as shown by the dashed line in Fig. 2. Since only $f^+(t)$ value is required when a positive peak occurs, the function f_k^+ is defined by sampling $f^+(t)$ in the instants when the positive peaks of the phases occur (see Fig. 2). Then

$$f_k^+ = \begin{cases} 1 - \dfrac{2k}{(1-D)N}, & \text{if } 0 \le k < N(1-D) \\ -1 + \dfrac{2k}{DN} - \dfrac{2(1-D)}{D}, & \text{if } N(1-D) < k \le N-1. \end{cases} \tag{3}$$

By using this representation, Fig. 3 illustrates the phases ripple and the total current ripple for a switching period. Notice that each phase current ripple has its own k index, with the origin in its respective positive peak. From this figure, it can be inferred that P_x^+ is given by

$$\begin{aligned} P_x^+ &= A_x f_0^+ + A_{x-1} f_1^+ \cdots + A_1 f_3^+ + A_0 f_4^+ \\ &\quad + A_{N-1} f_5^+ + \cdots + A_{x+1} f_{N-1}^+ \\ &= \sum_{k=0}^{N-1} A_{x-k} \cdot f_k^+ . \end{aligned} \tag{4}$$

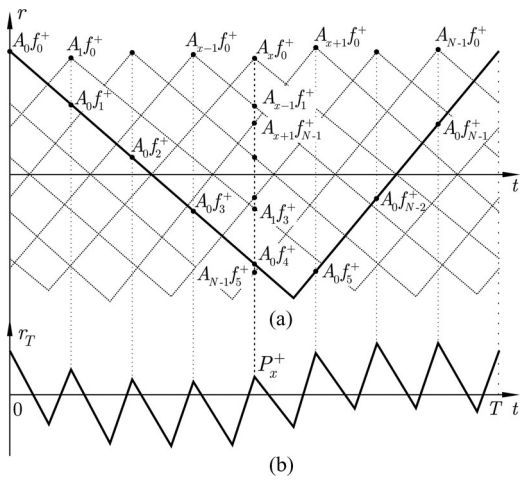

Fig. 3. Interleaved power converter. (a) Phase current ripple. (b) Total current ripple.

Notice that in (4), $x - k$ could become negative. In such case, due to the system periodicity, $x - k + N$ should be considered.

Operating with (3) and (4), the expression for P_x^+ is obtained

$$\begin{aligned} P_{x(D)}^+ &= \sum_{k=0}^{N-1} A_{x-k} \cdot f_k^+ = \sum_{k=0}^{N-1} A_{(x-k)} \left[1 - \frac{2k}{(1-D)N} \right] \\ &\quad + \sum_{k > N(1-D)}^{N-1} A_{(x-k)} \left[\frac{2k}{(1-D)DN} - \frac{2}{D} \right]. \end{aligned} \tag{5}$$

In the case of negative peaks, P_x^-, it is convenient to express the function $f(t)$ with its maximum negative on $t = 0$. This function, named $f^-(t)$, is represented by two sections with different slopes, separated by the instant $t = DT$. Operating in the same way as P_x^+, the expression for P_x^- can be obtained

$$\begin{aligned} P_{x(D)}^- &= \sum_{k=0}^{N-1} A_{x-k} \cdot f_k^- = -\sum_{k=0}^{N-1} A_{(x-k)} \left[1 - \frac{2k}{DN} \right] \\ &\quad - \sum_{k > N \cdot D}^{N-1} A_{(x-k)} \left[\frac{2k}{(1-D)DN} - \frac{2}{(1-D)} \right]. \end{aligned} \tag{6}$$

Analyzing (5) and (6), it can be noticed that the summands in the first sum are valid for any k, while in the second sum, due to the piecewise nature of f and the relationship between k and D, only the summands that verify the expression in the limits of the sum are valid. It is worth considering that the values of D determining the validity zone of each section are coincident with the cases of ripple cancellation in the ideal case.

It should be noticed that, due to the nonlinear relationship between the magnetic field and the inductor current, the L_x used to calculate A_x can change with the current. In such case, to calculate expressions (5) and (6), the peak amplitudes of each phase should be evaluated taking into account their current dependence. In some cases, such as in current-source applications, current dependence is associated with duty cycle dependence. Then, the A_x value will change with D, and has to be updated in each computation of (5) and (6) based on the relationship

between L_x and D. In other cases, where the total current does not affect the steady-state duty cycle, e.g., voltage regulators under different loads, the A_x value to be used in (5) and (6) has to be computed according to its current dependence and is valid for every D. Hence, computing these expressions for several current values leads to a family of curves.

III. Some Applications of the Proposed Method

Knowing the numerical value and the sequence of appearance of $P_x^{\pm}$ allows us to characterize the total current ripple, which is useful when it comes to evaluating relevant aspects of the converter design. In this sense, this section presents the calculation of some of these aspects such as the maximum amplitude, the harmonic content, and the RMS value of the total current ripple, and the voltage variation that this ripple generates in the capacitor C connected to the common point of the phases. These parameters, which are used to define C size and technology, impact on the power loss and voltage ripple in the capacitor. With respect to the harmonic content, if the N-phase converter is ideal, the first $N-1$ ripple harmonics are canceled relaxing the total current filtering specifications. However, in the nonideal case, this benefit is degraded, and consequently, an analysis of the first $N-1$ harmonics becomes necessary. This section lies on the proposed method to determine the analytic expressions of the aforementioned parameters.

A. Maximum Total Current Ripple Amplitude

The maximum value of the total current ripple can be obtained as a function of the duty cycle, $P_T(D)$. The procedure relies on the calculation of the ripple peaks produced by each phase current peak for different values of D, i.e., $P_x^{\pm}(D)$ for $x = 0, 1, \ldots, N-1$, using (5) and (6), respectively. Then, the maximum ripple is obtained by considering the maximum value of $P_i^{\pm}$ for a given D, as indicated in the following:

$$P_T(D) = \max\left(|P^+_{x(D)}|, |P^-_{x(D)}|\right). \tag{7}$$

This equation evaluates the absolute value of the ripple, so that the amplitude of the total ripple can be analyzed regardless of the $P_x^{\pm}$ sign. As an example, the maximum total current ripple for the particular case of three-phase interleaved buck and boost converters was computed. The normalized total ripple was obtained using (5)–(7), and the total ripple for each particular converter was derived from $\hat{I}_n$ in Table I. In both cases, the main parameters are: $L_1 = 280.5\mu\text{H}, L_2 = 255\mu\text{H}, L_3 = 242\mu\text{H}$, $f_{sw} = 12.21\text{kHz}$, and input voltage $V_i = 50\text{V}$. Fig. 4 displays the obtained results together with the ideal case, where the loss of the cancellation points can be noted.

B. RMS Value of the Total Current Ripple

The RMS value of the total current ripple can be calculated as

$$r_{T\text{rms}} = \sqrt{\frac{1}{T}\int_0^T [r_T(\tau)]^2\, d\tau} \tag{8}$$

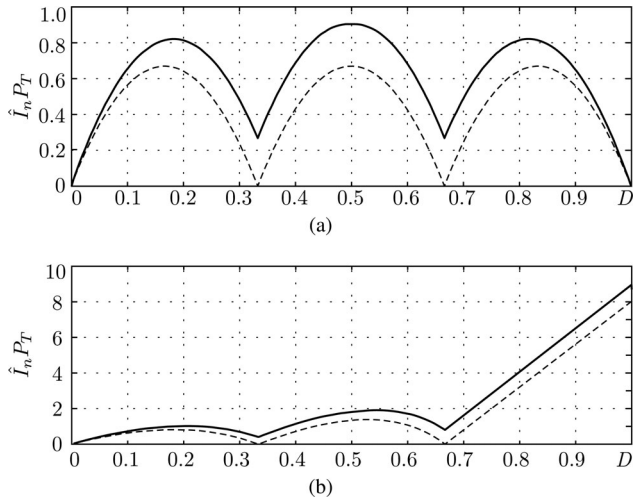

Fig. 4. Output current ripple. Ideal case (dashed). Non ideal case (solid). (a) Buck converter. (b) Boost converter.

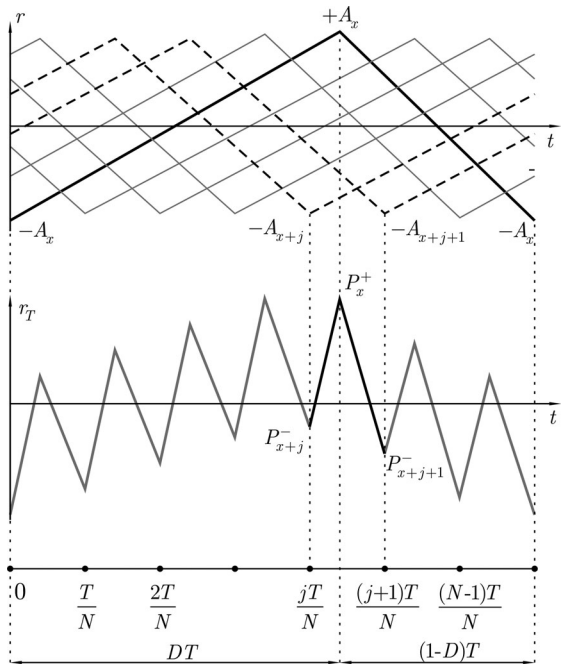

Fig. 5. Normalized RMS value calculation.

where r_T is the expression corresponding to the total current ripple, whose value in the peaks is given by the previously calculated $P_x^{\pm}$. Knowing these values allows us to segment the calculation of the RMS value in intervals. Then, the total RMS value is the sum of all the RMS values calculated in each interval. For this calculation, the intervals were defined as including a positive peak and being delimited by the appearance of two consecutive negative peaks, as shown in Fig. 5. This figure displays the phases ripple and the total ripple, where the interval including the positive peak associated with the phase x is highlighted. This positive peak, which is related to the instant DT, is located inside the interval given by $\frac{jT}{N} \le DT < \frac{(j+1)T}{N}$. Thus, P_x^+ is located between the negative peaks of the total current P^-_{x+j} and P^-_{x+j+1}, as illustrated in the figure.

The expression of RMS current ripple in this interval is shown as

$$r_{T\mathrm{rms}(x,D)} = \sqrt{\frac{1}{T}\left[\int_{\frac{jT}{N}}^{DT} [r_T^p(\tau)]^2\, d\tau + \int_{DT}^{\frac{(j+1)T}{N}} [r_T^n(\tau)]^2\, d\tau\right]} \tag{9}$$

with

$$\begin{aligned} r_T^p(\tau) &= m^p\,(\tau - t_0^p) + q^p \\ r_T^n(\tau) &= m^n\,(\tau - t_0^n) + q^n \end{aligned} \tag{10}$$

$$m^p = \frac{P_x^+ - P_{x+j}^-}{DT - \frac{jT}{N}} = q^p P_{x+j}^- = t_0^p \frac{jT}{N}$$

$$m^n = \frac{P_{x+j+1}^- - P_x^+}{\frac{(j+1)T}{N} - DT} = q^n P_x^+ = t_0^n DT \tag{11}$$

where r_T^p and r_T^n are the expressions corresponding to the total current ripple in this interval for the positive and negative slope, respectively. From Fig. 5, it can be noticed that j value is not arbitrary, but changes based on DT value. Since $DT > \frac{jT}{N}$ in the interval under analysis and j is an integer, then, j is the largest integer less than or equal to ND. This relationship can be expressed as

$$j = \max\{j \in \mathbb{Z} \mid j \le ND\}. \tag{12}$$

Then, the RMS value of the total current ripple as a function of the duty cycle is obtained by adding up the previous results of all the intervals, as shown in the following:

$$r_{T\mathrm{rms}_{(D)}} = \sqrt{\sum_{x=0}^{N-1} r_{\mathrm{rms}(x,D)}^2}$$

$$r_{T\mathrm{rms}_{(D)}}^2 = \sum_{x=0}^{N-1}\left(\frac{ND-j}{3N}\left[(P_x^+ - P_{x+j}^-)^2 + P_x^+\,P_{x+j}^-\right] + \frac{1-ND+j}{3N}\left[(P_x^+ - P_{x+j+1}^-)^2 + P_x^+\,P_{x+j+1}^-\right]\right). \tag{13}$$

Notice that (13) is only a function of D, since j is related to D by (12).

C. Maximum Voltage Ripple Across the Capacitor

Knowing $P_x^{\pm}$ allows us to calculate the voltage ripple across the capacitor connected to the common point of the phase inductors, i.e., at the input or at the output depending on the converter topology. In the following, it is assumed that the ripple of the total current mainly flows through the capacitor.

The voltage ripple, $\Delta v(t)$, can be calculated by using

$$\Delta v(t) = \frac{1}{C}\int_{t_0}^{t} \hat{I}_n r_T(\tau)\, d\tau + \left(\Delta v(t_0) - \hat{I}_n r_T(t_0) ESR\right) + \hat{I}_n r_T(t) ESR \tag{14}$$

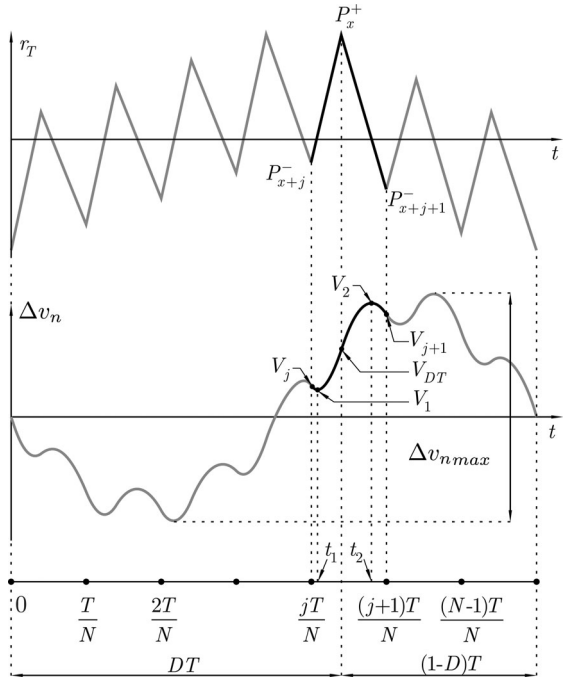

Fig. 6. Normalized voltage ripple calculation.

where ESR is the capacitor series resistance. The normalized version of Δv, defined as Δv_n, is shown as

$$\Delta v_n(t) = \frac{\Delta v(t)}{\hat{I}_n Z_n} = \frac{1}{Z_n C}\int_{t_0}^{t} r_T(\tau)\, d\tau + \Delta v_n(t_0) + \left[r_T(t) - r_T(t_0)\right] ESR_n \tag{15}$$

where $Z_n = (2\pi f_{sw} C)^{-1}$ is the impedance of the capacitor at $f_{sw} = \frac{1}{T}$ and $ESR_n = \frac{ESR}{Z_n}$ is the normalized ESR. The maximum voltage swing across the capacitor, $\Delta v_{n\max}$, is obtained for each D value and calculated from the difference between the maximum and the minimum values of $\Delta v_n(t)$ in a commutation period

$$\Delta v_{n\max}(D) = \max(\Delta v_n) - \min(\Delta v_n). \tag{16}$$

For a given D, (16) is calculated using the same methodology as in the calculation of the RMS current ripple, i.e., the voltage ripple across the capacitor is analyzed by intervals. In each interval, the maximum and minimum $\Delta v_n(t)$ values are computed, and then, $\Delta v_n \max$ is obtained by evaluating the maximum and minimum of all the intervals. To determine the maximum and minimum voltage inside each interval, $\Delta v_n(t)$ should be calculated for different points. These points allow us to concatenate the results of the different intervals and to establish the potential absolute maximum and minimum. Fig. 6 shows the total current ripple and the voltage ripple across the capacitor, Δv_n, where the interval associated with phase x is highlighted and the voltage corresponding to the previously mentioned points is shown. These points are: voltage at the beginning of the interval (V_j), voltage at time t_1 (V_1), voltage in the instant of change in the slope of r_T (V_{DT}), voltage at time t_2 (V_2), and voltage at the end of the interval (V_{j+1}). Note that the initial value of the voltage in the analyzed interval is the same as the voltage at the

end of the previous interval. Moreover, since t_1 and t_2 are the times corresponding to potential maximum or minimum values, they are obtained by making the first derivative of $\Delta v_n(t)$ equal to zero.

The expressions that allow us to calculate the different values of the voltage ripple, starting from an initial voltage V_j, are shown as follows:

$$\begin{aligned}
V_1 &= \frac{1}{Z_n C}\int_{\frac{jT}{N}}^{t_1}\left[m^p\left(\tau-\frac{jT}{N}\right)+q^p\right]d\tau \\
&\quad + V_j + m^p\left(t_1-\frac{jT}{N}\right)ESR_n \\
V_{DT} &= \frac{1}{Z_n C}\int_{\frac{jT}{N}}^{DT}\left[m^p\left(\tau-\frac{jT}{N}\right)+q^p\right]d\tau \\
&\quad + V_j + m^p\left(DT-\frac{jT}{N}\right)ESR_n \\
V_2 &= \frac{1}{Z_n C}\int_{DT}^{t_2}\left[m^n\left(\tau-DT\right)+q^n\right]d\tau \\
&\quad + V_{DT} + m^n\left(t_2-DT\right)ESR_n \\
V_{j+1} &= \frac{1}{Z_n C}\int_{DT}^{\frac{(j+1)T}{N}}\left[m^n\left(\tau-DT\right)+q^n\right]d\tau \\
&\quad + V_{DT} + m^n\left(\frac{(j+1)T}{N}-DT\right)ESR_n. \quad (17)
\end{aligned}$$

In the interval under analysis, Δv_n could be monotonic; in such case, times t_1 or t_2 do not exist, and the described equations cannot be used for the calculation of V_1 and V_2. If time t_1 does not exist, V_1 is then defined as $V_1 = V_j$, whereas if time t_2 does not exist, V_2 is defined as $V_2 = V_{j+1}$. The values for t_1 and t_2 can be calculated from the following equation, if they exist:

$$\begin{aligned}
t_1 &= \frac{jT}{N}-\left(\frac{q^p}{m^p}+ESR_n Z_n C\right) \\
t_2 &= DT-\left(\frac{q^n}{m^n}+ESR_n Z_n C\right). \quad (18)
\end{aligned}$$

Operating with (17) and (18), the calculation of the different voltages are obtained

$$\begin{aligned}
V_1 &= -\left(\frac{q^p}{Z_n C}+m^p ESR_n\right)^2\frac{Z_n C}{2m^p}+V_j \\
V_{DT} &= \left(DT-\frac{jT}{N}\right)\left[\frac{m^p}{2Z_n C}\left(DT-\frac{jT}{N}\right)\right. \\
&\quad \left.+\frac{q^p}{Z_n C}+m^p ESR_n\right]+V_j \\
V_2 &= -\left(\frac{q^n}{Z_n C}+m^n ESR_n\right)^2\frac{Z_n C}{2m^n}+V_{DT} \\
V_{j+1} &= \left(\frac{(j+1)T}{N}-DT\right)\left[\frac{m^n}{2Z_n C}\left(\frac{(j+1)T}{N}-DT\right)\right. \\
&\quad \left.+\frac{q^n}{Z_n C}+m^n ESR_n\right]+V_{DT}. \quad (19)
\end{aligned}$$

By evaluating (19) for each interval, the pair (V_1, V_2) is obtained and stored in vector V_C. Once the N intervals are evaluated, $\Delta v_{n\max}$ is calculated by considering the maximum and minimum vector values of V_C

$$\Delta v_{n\max}(D) = \max(V_C) - \min(V_C). \quad (20)$$

Below the procedure to compute $\Delta v_{n\max}$ is summarized:

1) for a given D, obtain j using (12);
2) update the index of the interval to be computed, i.e., x value;
3) given x and j values, and known the values of $P^{\pm}$, evaluate the expressions shown in (11);
4) evaluate (19) and store (V_1, V_2) in vector V_C;
5) repeat steps 2–4 until computing N intervals, i.e., evaluate from the interval corresponding to $x = 0$ to that of $x = N-1$;
6) obtain the maximum voltage swing across the capacitor using (20).

D. Harmonic Content of the Total Current Ripple

In this section, the harmonic content of the current ripple in the common point of the phase inductors is calculated as a function of $P_x^{\pm}$. This ripple can be written as a Fourier series, as shown in the following:

$$r_T(t) = \sum_{h=1}^{\infty}|r_{T\,h}|\cos\left(\frac{h2\pi t}{T}-\theta_h\right) \quad (21)$$

where

$$|r_{T\,h}| = \sqrt{a_h^2+b_h^2} \quad (22)$$

being a_h and b_h the real and imaginary parts of the hth component, respectively, which are calculated as follows:

$$\begin{aligned}
a_h &= \frac{2}{T}\int_0^T r_T(t)\cos\left(\frac{h\pi t}{T}\right)dt \\
b_h &= \frac{2}{T}\int_0^T r_T(t)\sin\left(\frac{h\pi t}{T}\right)dt. \quad (23)
\end{aligned}$$

As proposed in Section III-B, $r_T(t)$ function can be segmented, so as to include a positive peak in each segment and be delimited by the appearance of two consecutive negative peaks $\left(\frac{xT}{N}\le t\le\frac{(x+1)T}{N}\right)$, in order to calculate (23) by intervals, as

TABLE II
EXPRESSION FOR P_x^+ AS A FUNCTION OF D

$P_0^+(D)$	Condition
$A_0 - A_1\frac{(D+1/3)}{(1-D)} - A_2\frac{(D-1/3)}{(1-D)}$	$0 < D < 1/3$
$A_0 + A_1\frac{(D-2/3)}{D} - A_2\frac{(D-1/3)}{(1-D)}$	$1/3 < D < 2/3$
$A_0 + A_1\frac{(D-2/3)}{D} + A_2\frac{(D-4/3)}{D}$	$2/3 < D < 1$
$P_1^+(D)$	Condition
$-A_0\frac{(D-1/3)}{(1-D)} + A_1 - A_2\frac{(D+1/3)}{(1-D)}$	$0 < D < 1/3$
$-A_0\frac{(D-1/3)}{(1-D)} + A_1 + A_2\frac{(D-2/3)}{D}$	$1/3 < D < 2/3$
$A_0\frac{(D-4/3)}{D} + A_1 + A_2\frac{(D-2/3)}{D}$	$2/3 < D < 1$
$P_2^+(D)$	Condition
$-A_0\frac{(D+1/3)}{(1-D)} - A_1\frac{(D-1/3)}{(1-D)} + A_2$	$0 < D < 1/3$
$A_0\frac{(D-2/3)}{D} - A_1\frac{(D-1/3)}{(1-D)} + A_2$	$1/3 < D < 2/3$
$A_0\frac{(D-2/3)}{D} + A_1\frac{(D-4/3)}{D} + A_2$	$2/3 < D < 1$
$P_0^-(D)$	Condition
$-A_0 + A_1\frac{(D-1/3)}{(1-D)} + A_2\frac{(D+1/3)}{(1-D)}$	$0 < D < 1/3$
$-A_0 + A_1\frac{(D-1/3)}{(1-D)} - A_2\frac{(D-2/3)}{D}$	$1/3 < D < 2/3$
$-A_0 + A_1\frac{(D-4/3)}{D} - A_2\frac{(D-2/3)}{D}$	$2/3 < D < 1$
$P_1^-(D)$	Condition
$A_0\frac{(D+1/3)}{(1-D)} - A_1 + A_2\frac{(D-1/3)}{(1-D)}$	$0 < D < 1/3$
$-A_0\frac{(D-2/3)}{D} - A_1 + A_2\frac{(D-1/3)}{(1-D)}$	$1/3 < D < 2/3$
$-A_0\frac{(D-2/3)}{D} - A_1 - A_2\frac{(D-4/3)}{D}$	$2/3 < D < 1$
$P_2^-(D)$	Condition
$A_0\frac{(D-1/3)}{(1-D)} + A_1\frac{(D+1/3)}{(1-D)} - A_2$	$0 < D < 1/3$
$A_0\frac{(D-1/3)}{(1-D)} - A_1\frac{(D-2/3)}{D} - A_2$	$1/3 < D < 2/3$
$-A_0\frac{(D-4/3)}{D} - A_1\frac{(D-2/3)}{D} - A_2$	$2/3 < D < 1$

shown in the following:

$$a_h = \sum_{x=0}^{N-1}\frac{2}{T}\int_{\frac{xT}{N}}^{\frac{(x+1)T}{N}} r_{_T}(t)\cos\left(\frac{h\pi t}{T}\right)dt = \sum_{x=0}^{N-1}\frac{a_{hx}}{h\pi}$$
$$b_h = \sum_{x=0}^{N-1}\frac{2}{T}\int_{\frac{xT}{N}}^{\frac{(x+1)T}{N}} r_{_T}(t)\sin\left(\frac{h\pi t}{T}\right)dt = \sum_{x=0}^{N-1}\frac{b_{hx}}{h\pi}. \quad (24)$$

Then, by solving the integral terms for each segment and by simplifying the resulting expressions, a_{hx} and b_{hx} are

$$a_{hx} = (P_x^+ - P_{x+j+1}^-)\mathrm{sinc}\left(\frac{(j+1-ND)h\pi}{N}\right) \times \sin\left(\frac{(2x+ND+j+1)h\pi}{N}\right)$$

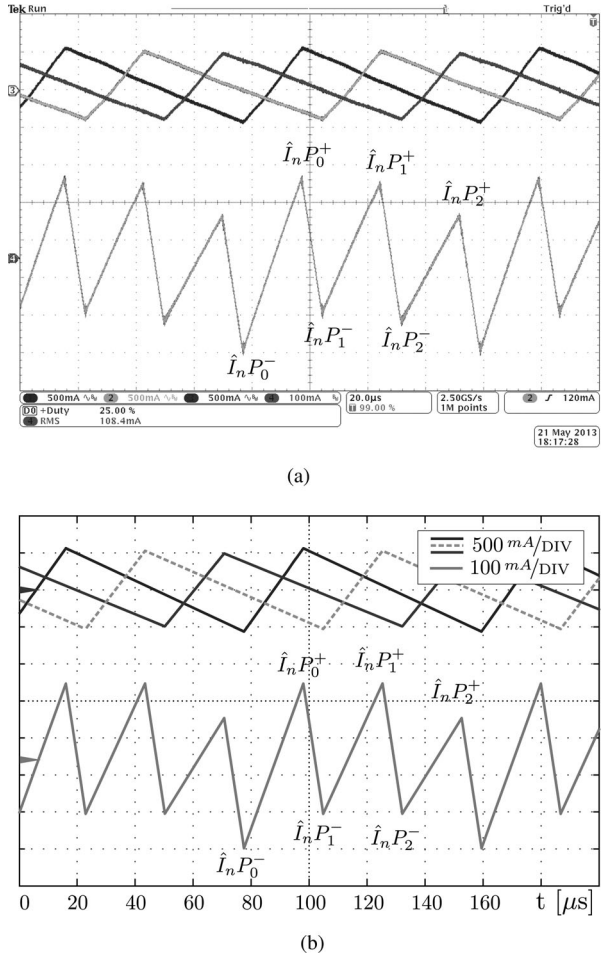

Fig. 7. Phase current and total ripple. Experimental and simulation results. (a) Experimental. (b) Simulated.

$$+ (P_{x+j}^- - P_x^+)\mathrm{sinc}\left(\frac{(j-ND)h\pi}{N}\right)\sin\left(\frac{(2x+ND+j)h\pi}{N}\right) + P_{x+j+1}^-\sin\left(\frac{2(x+j+1)h\pi}{N}\right) - P_{x+j}^-\sin\left(\frac{2(x+j)h\pi}{N}\right) \quad (25)$$

$$b_{hx} = (P_x^+ - P_{x+j+1}^-)\mathrm{sinc}\left(\frac{(j+1-ND)h\pi}{N}\right) \times \cos\left(\frac{(2x+ND+j+1)h\pi}{N}\right) + (P_{x+j}^- - P_x^+)\mathrm{sinc}\left(\frac{(j-ND)h\pi}{N}\right)\cos\left(\frac{(2x+ND+j)h\pi}{N}\right) + P_{x+j+1}^-\cos\left(\frac{2(x+j+1)h\pi}{N}\right) - P_{x+j}^-\cos\left(\frac{2(x+j)h\pi}{N}\right). \quad (26)$$

Once a_{hx} and b_{hx} are computed for each h and D, (22) can be computed through (24).

TABLE III
EXPERIMENTAL RESULTS

	$D = 0.25,\ V_{in} = 17.8\,\mathrm{V},\ \hat{I_n} = 0.539\,\mathrm{A}$	
$\hat{I_n} P_x$	Calculated [mA]	Measured [mA]
$\hat{I_n} P_0^+$	206	210
$\hat{I_n} P_1^+$	207	197
$\hat{I_n} P_2^+$	113	112
$\hat{I_n} P_0^-$	-238	-241
$\hat{I_n} P_1^-$	-145	-144
$\hat{I_n} P_2^-$	-144	-163

Denormalized $P_x^{\pm}$.

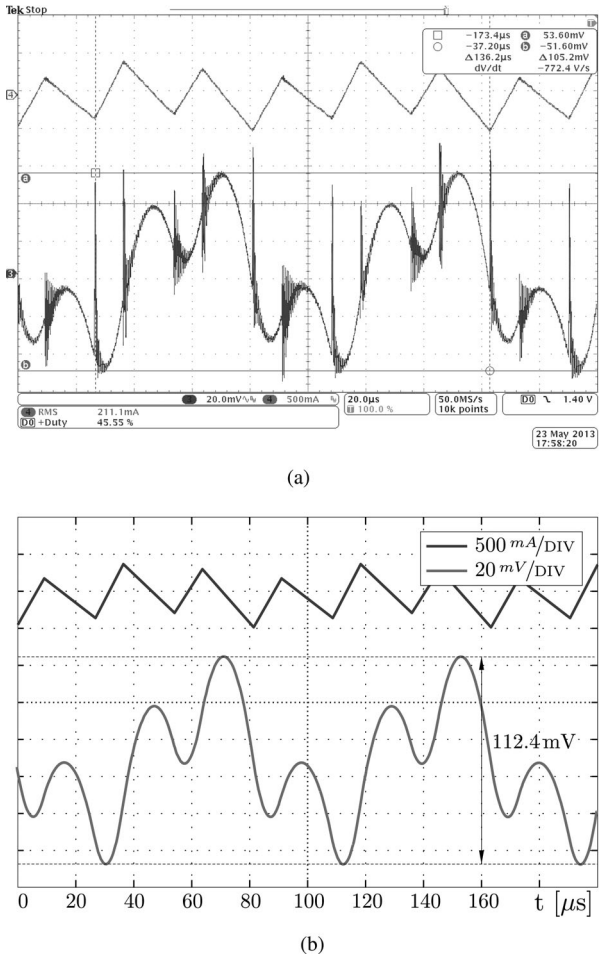

Fig. 8. Capacitor voltage ($D = 0.45$). Experimental and simulation results.

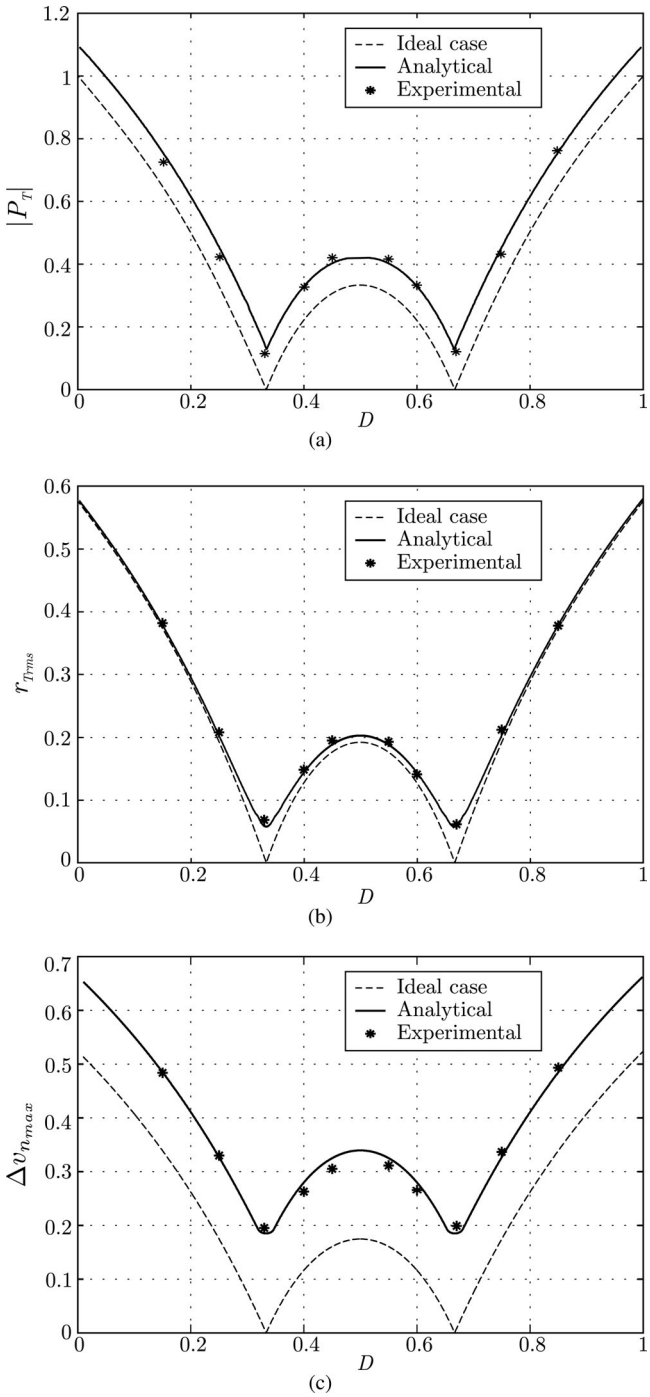

Fig. 9. Experimental results. (a) Normalized maximum ripple amplitude $|P_T|$. (b) Normalized total rms current ripple $r_{T\,\mathrm{rms}}$. (c) Normalized capacitor maximum voltage ripple $\Delta v_{n\,\mathrm{max}}$.

IV. EXPERIMENTAL RESULTS

In order to validate the proposed method and the described applications, experimental results on a three-phase interleaved buck converter were conducted and compared to the computed results of the expressions using MATLAB software. The main specifications are: commutation period $T = 81.9\mu$s (i.e., $f_{sw} = T^{-1} = 12.21$kHz) and output capacitor $C = 40\mu$F. The nominal phase inductance is sized according to the peak amplitude of the phase current ripple specified by the design, which was selected to be 1A. Since the maximum ripple occurs at $D = 0.5$ and considering $V_i = 25$V, the nominal phase inductance is

$$L_n = \frac{V_i(1-D)DT}{2\hat{I_n}} = 256\mu H. \tag{27}$$

The phase inductors are built with double-E gapped ferrite cores, leading to $\pm 7\%$ inductance tolerance: $L_0 = 239\ \mu$H, $L_1 = 255\mu$H, and $L_2 = 273\mu$H. The use of gapped inductors allows us to obtain approximately constant inductances in the evaluated current range, thereby A_x values were considered

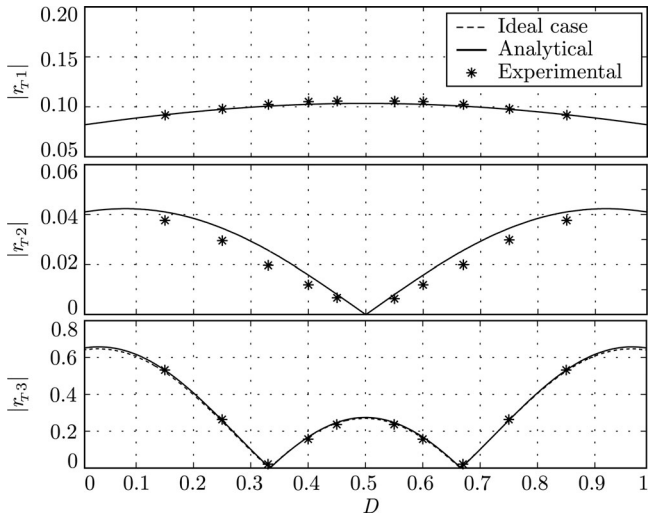

Fig. 10. Experimental results. Spectrum analysis.

constants for all D. The tolerances in the inductance produce mismatches in the amplitude of the phase ripples, leading to $A_0 = 1.07, A_1 = 1.004$, and $A_2 = 0.937$. Given the reduced number of phases, compact expressions for $P_x^{\pm}$ can be obtained by using (5) and (6). Table II shows the expressions for P_x.

Fig. 7 shows the experimental and simulated waveforms corresponding to the phase currents and the total current ripple obtained with $D = 0.25$. The peaks of the total current, which are the denormalized $P_x^{\pm}$, are identified in the figures. Table III summarizes the measured values, which are in close agreement with the calculated values.

The maximum voltage ripple was also evaluated. Fig. 8 displays the experimental and simulated waveforms of the total current ripple and the capacitor voltage ripple in the condition described. The case of $D = 0.45$ and $V_i = 28$V was calculated and then simulated, leading to a peak-to-peak voltage ripple of 112.4mV, as shown in Fig. 8(b), which corresponds to a normalized voltage ripple of $\Delta v_{Cn\max} = 0.325$. On the other hand, the experimental measured peak-to-peak voltage ripple is 105.2mV, as shown in Fig. 8(a), which corresponds to a normalized value of $\Delta v_{Cn\max} = 0.305$. Notice that the ringing present in the experimental voltage waveform is produced by the commutation noise being picked up by the parasitic inductances of the experimental and measurement setup.

The analytical expressions developed in Section III were validated by means of experimental measurements on the power converter. Fig. 9 shows the validation of (7), (13), and (20). It can be seen that the experimental results obtained are in close agreement with the analytical curves obtained with the proposed method. The ideal case is also included in the figure as a reference, in order to illustrate the difference between this case and the analyzed one. Additionally, Fig. 10 illustrates the validation of (22). It can be appreciated that, due to the inductance mismatch, the spectral lines corresponding to f_{sw} ($|r_{T\,1}|$) and $2f_{sw}$ ($|r_{T\,2}|$) are no longer canceled in the output current. As a consequence, the ripple cancellation points are lost in r_T, although they are still present in the spectral line corresponding to Nf_{sw} ($|r_{T\,3}|$).

V. Conclusion

The benefits of interleaved power converters are degraded, among other causes, by phase inductance mismatch. This mismatch can be caused by tolerances in the manufacturing process or in the core magnetic properties, leading to differences in phase ripples amplitudes. Consequently, compared to the ideal case, the total current ripple becomes significantly greater, and the switching frequency component and its harmonics are not canceled, which impacts on the overall system performance. This paper presents a general analysis method for the characterization of the steady-state total current ripple for any inductance mismatch. This characterization, based on the analysis of each phase ripple in the time domain, allows us to determine the peak values of the total current ripple and the instant in which these peaks appear. The proposal permits to obtain a general expression for the total current ripple for the whole duty cycle range, which enables to compute different characteristics related to this ripple with no need to simulate the converter for each value of the duty cycle. Using the proposed method, expressions for the maximum amplitude, the harmonic content, and the RMS value of the total current ripple, and the voltage variation that this ripple generates in the capacitor connected to the common point of the phases, were obtained. The proposal was experimentally validated by means of measurements on a three-phase interleaved buck converter, displaying an outstanding correlation with the analytical expressions developed.

References

[1] M. Abusara and S. Sharkh, "Design and control of a grid-connected interleaved inverter," *IEEE Trans. Power Electron.*, vol. 28, no. 2, pp. 748–764, Feb. 2013.

[2] L. Ni, D. Patterson, and J. Hudgins, "High power current sensorless bidirectional 16-phase interleaved dc-dc converter for hybrid vehicle application," *IEEE Trans. Power Electron.*, vol. 27, no. 3, pp. 1141–1151, Mar. 2012.

[3] O. Hegazy, J. Van Mierlo, and P. Lataire, "Analysis, modeling, and implementation of a multidevice interleaved dc/dc converter for fuel cell hybrid electric vehicles," *IEEE Trans. Power Electron.*, vol. 27, no. 11, pp. 4445–4458, Nov. 2012.

[4] H. Choi, "Interleaved boundary conduction mode (BCM) buck power factor correction (PFC) converter," *IEEE Trans. Power Electron.*, vol. 28, no. 6, pp. 2629–2634, Jun. 2013.

[5] J. Quintero, A. Barrado, M. Sanz, C. Fernandez, and P. Zumel, "Impact of linear nonlinear control in multiphase VRM design," *IEEE Trans. Power Electron.*, vol. 26, no. 7, pp. 1826–1831, Jul. 2011.

[6] R. Garcia Retegui, M. Benedetti, M. Funes, P. Antoszczuk, and D. Carrica, "Current control for high-dynamic high-power multiphase buck converters," *IEEE Trans. Power Electron.*, vol. 27, no. 2, pp. 614–618, Feb. 2012.

[7] W. Chen, "High efficiency, high density, polyphase converters for high current applications," Linear Technology, Milpitas, CA, USA: Application Note AN77, 1999.

[8] C. Chang and M. Knights, "Interleaving technique in distributed power conversion systems," *IEEE Trans. Circuits Syst. I*, vol. 42, no. 5, pp. 245–251, May 1995.

[9] S. Zhang and X. Yu, "A unified analytical modeling of the interleaved pulse-width-modulation (PWM) dc-dc converter and its applications," *IEEE Trans. Power Electron.*, vol. 28, no. 11, pp. 5147–5158, Nov. 2013.

[10] R. Foley, R. Kavanagh, and M. Egan, "Sensorless current estimation and sharing in multiphase buck converters," *IEEE Trans. Power Electron.*, vol. 27, no. 6, pp. 2936–2946, Jun. 2012.

[11] Y. Cho, A. Koran, H. Miwa, B. York, and J.-S. Lai, "An active current reconstruction and balancing strategy with DC-link current sensing for a multi-phase coupled-inductor converter," *IEEE Trans. Power Electron.*, vol. 27, no. 4, pp. 1697–1705, Apr. 2012.

[12] J.-T. Su and C.-W. Lin, "Auto-tuning scheme for improved current sharing of multiphase dc-dc converters," *IET Power Electron*., vol. 5, no. 9, pp. 1605–1613, Nov. 2012.
[13] S. Chae, Y. Song, S. Park, and H. Jeong, "Digital current sharing method for parallel interleaved DC-DC converters using input ripple voltage," *IEEE Trans. Ind. Informat*., vol. 8, no. 3, pp. 536–544, Aug. 2012.
[14] K. Hwu and Y. Chen, "Current sharing control strategy based on phase link," *IEEE Trans. Ind. Electron*., vol. 59, no. 2, pp. 701–713, Feb. 2012.
[15] Y. Zhang, M. Yu, F. Liu, and Y. Kang, "Instantaneous current-sharing control strategy for parallel operation of ups modules using virtual impedance," *IEEE Trans. Power Electron*., vol. 28, no. 1, pp. 432–440, Jan. 2013.
[16] L. Huber, B. Irving, and M. Jovanovic, "Open-loop control methods for interleaved DCM/CCM boundary boost PFC converters," *IEEE Trans. Power Electron*., vol. 23, no. 4, pp. 1649–1657, Jul. 2008.
[17] X. Xu, W. Liu, and A. Huang, "Two-phase interleaved critical mode PFC boost converter with closed loop interleaving strategy," *IEEE Trans. Power Electron*., vol. 24, no. 12, pp. 3003–3013, Dec. 2009.
[18] K.-M. Ho, C.-A. Yeh, and Y.-S. Lai, "Novel digital-controlled transition current-mode control and duty compensation techniques for interleaved power factor corrector," *IEEE Trans. Power Electron*., vol. 25, no. 12, pp. 3085–3094, Dec. 2010.
[19] H. Choi and L. Balogh, "A cross-coupled master slave interleaving method for boundary conduction mode (BCM) PFC converters," *IEEE Trans. Power Electron*., vol. 27, no. 10, pp. 4202–4211, Oct. 2012.
[20] Micrometals Iron Powder Cores. (2013). "Electronic references," [Online]. Available: http://www.micrometals.com/
[21] R. Lenk, in *Practical Design of Power Supplies*, R. F. Hoyt, Ed. New York, NY, USA: Wiley-IEEE Press, 2005.
[22] O. Garcia, A. de Castro, P. Zumelis, and J. Cobos, "Digital-control-based solution to the effect of nonidealities of the inductors in multiphase converters," *IEEE Trans. Power Electron*., vol. 22, no. 6, pp. 2155–2163, Nov. 2007.
[23] J. Abu-Qahouq, M. Batarseh, L. Huang, and I. Batarseh, "Analysis and small signal modeling of a non-uniform multiphase buck converter," in *Proc. IEEE Power Electron. Spec. Conf*., Jun. 2007, pp. 961–967.
[24] Y. Gu and D. Zhang, "Interleaved boost converter with ripple cancellation network," *IEEE Trans. Power Electron*., vol. 28, no. 8, pp. 3860–3869, Aug. 2013.

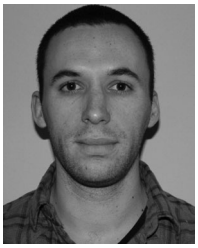

Pablo D. Antoszczuk (S'11) was born in Mar del Plata, Argentina, in 1985. He received the Electronics Engineering degree from the Universidad Nacional de Mar del Plata (UNMdP), Mar del Plata, in 2010, where he is currently working toward the Ph.D. degree in electronics engineering.

He is currently a Graduate Student Researcher at the National Scientific and Technical Research Council, Buenos Aires, Argentina. He is a Researcher at the Instrumentation and Control Laboratory (LIC, UNMdP). His research interests are in the fields of power converters, current control, and high precision measurements.

Rogelio Garcia Retegui (M'12) was born in Tandil, Argentina, in 1977. He received the Electronics Engineering degree and the Ph.D. degree in electronics engineering from the Universidad Nacional de Mar del Plata (UNMdP), Mar del Plata, Argentina, in 2002 and 2009, respectively.

He is currently with the Instrumentation and Control Laboratory (LIC, UNMdP), as a Researcher, and he is also an Assistant Researcher at the National Scientific and Technical Research Council, Buenos Aires, Argentina. Since 2003, he has been an Assistant Professor in the Control Theory and Control Systems course at the UNMdP. His current research interests include power electronics, current control, and pulsed power converters for particle accelerators.

Nicolas Wassinger (S'11) was born in Buenos Aires, Argentina, in 1984. He received the Electronics Engineering degree and the Ph.D. degree in electronics engineering from the Universidad Nacional de Mar del Plata (UNMdP), Mar del Plata, Argentina, in 2008 and 2012, respectively.

He is currently with the Instrumentation and Control Laboratory (LIC, UNMdP) as a Researcher. He is also an Assistant Professor in the Control Systems course at the UNMdP. Since 2008, he has been a member of the National Scientific and Technical Research Council, Buenos Aires, Argentina. His research interests are in the fields of power converters for particle accelerators and digital signal processing.

Sebastian Maestri was born in Mar del Plata, Argentina, in 1978. He received the Electronics Engineering degree and the Ph.D. degree from the Universidad Nacional de Mar del Plata (UNMdP), Mar del Plata, in 2005 and 2009, respectively.

He is currently with the the Instrumentation and Control Laboratory (LIC, UNMdP), as a Researcher, and he is also an Assistant Researcher at the National Scientific and Technical Research Council, Buenos Aires, Argentina. Since 2005, he has been an Assistant Professor in the Control Theory course at the UNMdP. His research interests include power electronics, pulsed power converters for particle accelerators, and line-commutated converters control.

Marcos Funes (M'12) was born in Mar del Plata, Argentina, in 1974. He received the Electronics Engineering degree and the Ph.D. degree from the Universidad Nacional de Mar del Plata (UNMDP), Mar del Plata, in 1999 and 2007, respectively.

In 1999, he joined the Department of Electronics, Universidad Nacional de Mar del Plata, as an Assistant Professor and a Research Assistant. Since 2009, he has been working for the National Scientific and Technical Research Council, Buenos Aires, Argentina as a Research Assistant. His current research interests include high-density programmable logic devices, power converters control, power line communication, and digital signal processing.

Mario Benedetti was born in Italy, in 1945. He received the degree in telecommunications engineering from the Universidad Nacional de La Plata (UNLP), La Plata, Argentina, in 1968.

From 1968 to 1983, he was with the Laboratory of Industrial Electronics, Control and Instrumentation, (LEICI, UNLP), where he developed electronic instruments. From 1970 to 1983, he was an Associate Professor in the Department of Electrical Engineering, UNLP. He spent two years as a Fellow at the Conseil Europeen pour la Recherche Nucleaire, Geneva, Switzerland. Since 1985, he has been a Full Professor in the Department of Electrical Engineering, Universidad Nacional de Mar del Plata (UNMdP), Mar del Plata, Argentina. He was the Director of the Instrumentation and Control Laboratory until 2012, Department of Electronics, UNMdP, and he is a member of the National Scientific and Technical Research Council, Buenos Aires, Argentina. He has served as a Lecturer at numerous short seminars granted to the industry sector and other universities. His current research interests include power electronics and electromagnetic compatibility.